Research Article Vol. 1, No. 9 / 15 Sep 2022 / Optics Continuum 2002
OPTICS CONTINUUM

# 10-cm spatial resolution distributed acoustic sensor based on an ultra low-loss enhanced backscattering fiber

ALI MASOUDI,* TIMOTHY LEE, MARTYNAS BERESNA, AND GILBERTO BRAMBILLA

*Optoelectronics Research Centre, University of Southampton, Southampton, SO17 1BJ, UK*
*a.masoudi@soton.ac.uk

**Abstract:** In this work, a distributed acoustic sensor (DAS) with 10-*cm* spatial resolution is demonstrated. Such a high resolution is achieved by employing an ultra low-loss enhanced backscattering (ULEB) fiber as a sensing element. A conventional DAS system is modified to interrogate the ULEB fiber comprised of 50 discrete reflectors with an average reflectance of $-56\,dB$. The ULEB fiber was fabricated with an automated reel-to-reel inscription machine, modified to create more uniform reflectors with similar reflectivity in the core of the fiber. The sensing arrangement exhibits a phase noise of $1.9\,n\varepsilon/\sqrt{Hz}$ over $1\,km$ sensing range.



## 1. Introduction

The past decade has witnessed a rapid adoption of distributed acoustic sensor (DAS) technology in various fields from geophysical sciences [1–3] and railway track behavior analysis [4] to hydrocarbon reservoir monitoring [5,6] and submarine power cable condition assessment [7,8]. Thus far, most of the research efforts in DAS technology have been devoted to addressing the requirements of the oil and gas industry which accounts for the largest share of the DAS market, requirements such as systems with a longer sensing range [9–11] and higher measurement accuracy [12–15]. Consequently, less effort has been directed towards improving the spatial resolution of DAS systems. With $1\,m$ gauge length providing sufficient spatial resolution for DASs main target market, commercial DAS manufacturers have had little incentive to use shorter probe pulses to achieve sub-meter resolution by sacrificing the signal-to-noise ratio (SNR). This, in turn, has restricted the adoption of DAS technology in areas such as mechanical and civil engineering which require mapping dynamic strains with much higher resolution.

The most commonly used approach to obtain a high resolution map of dynamic strains along a structure is based on fiber Bragg grating (FBG) arrays [16,17]. In this approach, several tens of FBGs with different Bragg wavelengths are used to measure strain levels at multiple points along the fiber. The number of sensing nodes in such an array, however, is usually limited to less than a hundred per fiber which may restrict the application of this approach. To address this limitation, sensing systems based on ultra-weak fiber Bragg grating (UWFBG) arrays have been developed [18–21]. UWFBG arrays, used in this approach, are comprised of several hundred low-reflectivity FBGs with an identical Bragg wavelength which, unlike conventional FBG arrays, are interrogated through time division multiplexing. Using this approach, Li et al. [22] have demonstrated a $2\,km$ long sensing system based on an array of 960 UWFBGs with $-40\,dB$ reflectivity capable of measuring dynamic strain with frequencies as high as $12.5\,kHz$. Despite exhibiting a superior strain accuracy, sensing systems that rely on UWFBG array are susceptible to signal fading due to slow drift in the Bragg wavelength of the FBGs as a result of localized temperature or strain changes. Any such drifts in the Bragg wavelength of the FBGs that pushes

#468673 https://doi.org/10.1364/OPTCON.468673
Journal © 2022 Received 23 Jun 2022; revised 22 Jul 2022; accepted 24 Jul 2022; published 8 Sep 2022

OPTICS CONTINUUM

their reflection bands beyond the operating wavelength of the seed laser will result in signal fading.

Several studies have shown that DAS systems based on phase-sensitive optical time-domain reflectometry ($\phi$-OTDR) can achieve sub-meter spatial resolution by either sacrificing the sensitivity or using very high speed digitizers [23–26]. For instance, using 5 $ns$ probe pulses, Masoudi et al. [23] have demonstrate a DAS system with 50 $cm$ spatial resolution albeit with a minimum detectable strain amplitude of 40 $n\varepsilon$ at 200 $Hz$. In 2018, Chen et al. [25] used a chirped-pulse $\phi$-OTDR to achieve 80 $cm$ spatial resolution over 9.8 $km$ sensing range. Although the setup achieved an excellent strain sensitivity of 245 $p\varepsilon/\sqrt{Hz}$, it relied on a 2 $GHz$ bandwidth oscilloscope and linear frequency modulation of up to 1 $GHz$ to achieve a sub-meter spatial resolution. An extreme example of this approach was demonstrated by Martins et al. [26] where an oscilloscope with 62 $GHz$ bandwidth was used to demonstrate a DAS with 2.5 $cm$ spatial resolution. Although these examples show that $\phi$-OTDR can achieve sub-meter resolution along conventional telecom optical fiber, using high frequency electronics to achieve such high resolutions might be prohibitively expensive in many applications.

Other interrogation techniques such as optical frequency-domain reflectometry (OFDR) have also been used to obtain a high-resolution map of dynamic strains along sensing fibers [27–30]. In this approach, the strain distribution along the sensing fiber is obtained by extracting the phase of the Rayleigh backscattered light from OFDR traces and calculating the changes in the value of the differential phase between adjacent points along the fiber. This interrogation technique has been used to demonstrate DAS with a spatial resolution as low as 10 $cm$ over a sensing range of 200 $m$. The main limitation of OFDR interrogation technique, however, is its trade-off between the measurement accuracy and spatial resolution [31].

Recently, a new class of specialty optical fibers has been developed that can enhance the backscattered signal by more than 20 $dB$ above the naturally occurring Rayleigh backscattered signal. The enhancement in the intensity of the backscattered signal has been achieved by either forming a continuous grating along the fiber [32] or inscribing individual reflectors at fixed intervals in the core of the fiber [33]. In 2020, Zhang et al. [34] have shown that the spatial resolution of a conventional DAS system that operates based on $\phi$-OTDR interrogation technique can be reduced to as low as 20 $cm$ if a continuous grating enhanced backscattering (CGEB) fiber is used as a sensing medium. In the following year, Xiong et al. [35] have used CGEB fiber to demonstrate a DAS system with 28 $cm$ resolution, but over a much longer sensing range of up to 920 $m$. Despite these successful demonstrations, since the intensity of the backscattered light in a CGEB fiber is proportional to the duration of the probe pulse, DAS systems based on CGEB fiber still encounter the same trade-off between the spatial resolution and SNR. Additionally, the enhancement in the intensity of the backscattered signal in CGEB fiber comes at the cost of higher attenuation level which, in turn, affects the sensing range of the sensor. Enhanced backscattering fibers based on point reflectors, on the other hand, does not suffer from the aforementioned trade-offs. This class of fibers, which are also known as ultra low-loss enhanced backscattering (ULEB) fibers, combines the advantages of UWFBG array and CGEB fiber to form a sensing medium that is capable of boosting the backscattered signal by more than 20 $dB$, has an extremely low excess loss (down to 0.01 $dB$ excess loss per 100 reflectors [36]), and is wavelength independent. So far, ULEB fibers have been used to extend the sensing range and measurement precision of conventional DAS systems [36,37]. In this letter, a ULEB fiber with 50 reflectors, spaced 10 $cm$ apart, is used to demonstrate a high-resolution DAS based on $\phi-$OTDR interrogation technique. It is shown that such an arrangement can achieve a sensing range and measurement accuracy of 1 $km$ and 1.9 $n\varepsilon/\sqrt{Hz}$, respectively.

OPTICS CONTINUUM

## 2. Principle

The sensing principle of the DAS setup, used in this study, is based on using a Mach-Zehnder interferometer (MZI) with a fixed path-imbalance to measure the phase difference between adjacent points along the sensing fiber. The role of the interferometer is to mix the backscattered light from different points on the sensing fiber by splitting the backscattered signal into two paths and combining them back with a fixed temporal delay. For an interferometer with a path difference of $\Delta L$, the intensity at the output of the interferometer is given by [23]:

$$I = A + B\cos(\beta\Delta L + \Delta\Phi) \tag{1}$$

where $\beta$ is the propagation constant of the probe pulse, $\Delta\Phi$ is the phase difference between two separate points on the fiber, and $A$ and $B$ are determined by the intensity of the backscattered light. Since the gauge-length of the sensing arrangement, used in this study, is dictated by the spatial separation between the reflectors in the ULEB fiber, the path-imbalance of the MZI should be fixed to twice the distance between the reflectors. In order to avoid phase fading while extracting the phase information from Eq. (1), a symmetric $3 \times 3$ coupler can be used at the output of the interferometer. The data from three arms of the $3 \times 3$ coupler can then be combined to yield [38]:

$$\Delta\Phi = 0.78 \times \varepsilon\ell\frac{4\pi n}{\lambda} \tag{2}$$

where $\varepsilon$ is the induced strain at a given section of the sensing fiber, $\ell$ is the length of that section, $n$ is the effective refractive index of the fiber, and $\lambda$ is the wavelength of the seed laser. Equation (2) shows that the phase-difference between the backscattered light from two adjacent reflectors has a linear relationship with the induced strain between those reflectors.

## 3. Experiment

### 3.1. Sensing setup

The sensing arrangement is shown in Fig. 1. A narrow linewidth DFB laser diode ($\lambda = 1550\,nm$, $\Delta\nu = 100\,kHz$) is used as a seed laser. The laser output is intensity modulated by an electro-optic modulator (EOM) to generate $500\,ps$ probe pulses with $25\,kHz$ repetition rate. To increase the extinction ratio of the probe pulses, a semiconductor optical amplifier (SOA) is employed as a pulse picker followed by a dense wavelength division multiplexing (DWDM) filter with $100\,GHz$ bandwidth to limit the forward amplified spontaneous emission (ASE) of the SOA. As a high-speed optical switch, the SOA plays an important role in generating a high extinction-ratio probe pulse with short pedestal. The probe pulse with $5\,mW$ peak power is launched into the fiber under test (FUT) via circulator C1.

A $5\,m$ long ULEB fiber with 50 point reflectors is spliced to $990\,m$ long standard single-mode fiber (SSMF) to form the FUT. A $50\,mm$ long piezoelectric stacks (Thorlabs: PK4FXH3P2) is attached to the ULEB fiber between its $48^{\text{th}}$ and $49^{\text{th}}$ reflectors, i.e. the second to last channel of the ULEB fiber, to generate test signals. An extra $5\,m$ of SSMF is added after the ULEB fiber to separate it from the far-end of the FUT.

At the receiving arm of the sensing system, the backscattered signal from the FUT is first amplified by an Erbium-doped optical amplifier (EDFA) and filtered by an FBG filter ($\lambda_B = 1550.1\,nm$, $\Delta\lambda = 0.2\,nm$, Reflectivity = 99%) to minimize the ASE. The amplified backscattered light is then passed through a MZI with $20\,cm$ path imbalance to mix the back-reflected signals from adjacent reflectors. Finally, the mixed signal at the output of the interferometer is detected by three amplified photodetectors ($BW = 600\,MHz$, $TIA = 40\,k\Omega$) and sampled with a $500\,MHz$ bandwidth PCIe digitizer at a rate of $1.25\,GS/s$. The captured data is then analyzed using Arctan demodulation algorithm [23] to extract the phase information.

OPTICS CONTINUUM

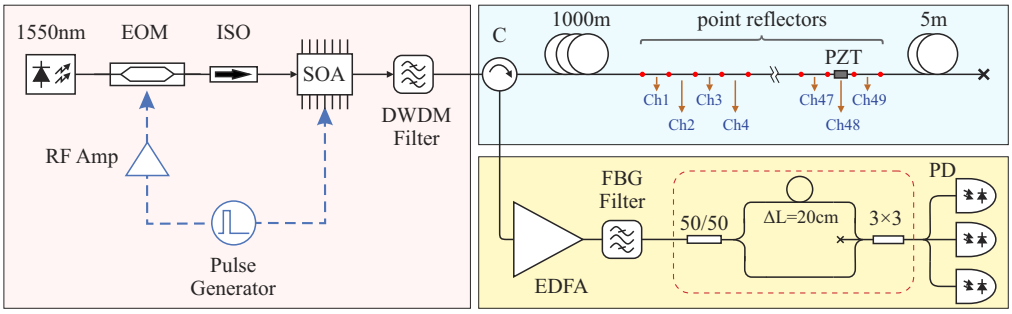


**Fig. 1.** Sensing setup of high-resolution DAS based on ULEB fiber. EOM: Electro-optic modulator; ISO: isolator; SOA: Semiconductor optical amplifier; DWDM: Dense wavelength division multiplexing; PZT: Piezo-electric actuator; C: Circulator; EDFA: Erbium-doped fiber amplifier; FBG: fiber Bragg grating; IMZI: Imbalanced Mach–Zehnder interferometer; PD: Photodetector; Data Acq.: Data acquisition unit. The red dots along the sensing fiber represent the point reflectors.

### 3.2. *ULEB fiber inscription setup*

The ULEB fiber, used in this test, was fabricated using an automated reel-to-reel fiber inscription setup, a schematic of which is shown in Fig. 2(a). An objective lens was used to focus the output of a femtosecond laser with pulse duration and energy of 200 $fs$ and 4 $\mu J$, respectively, on the target fiber. Data from a CCD camera was used to automatically align the fiber at the focal point

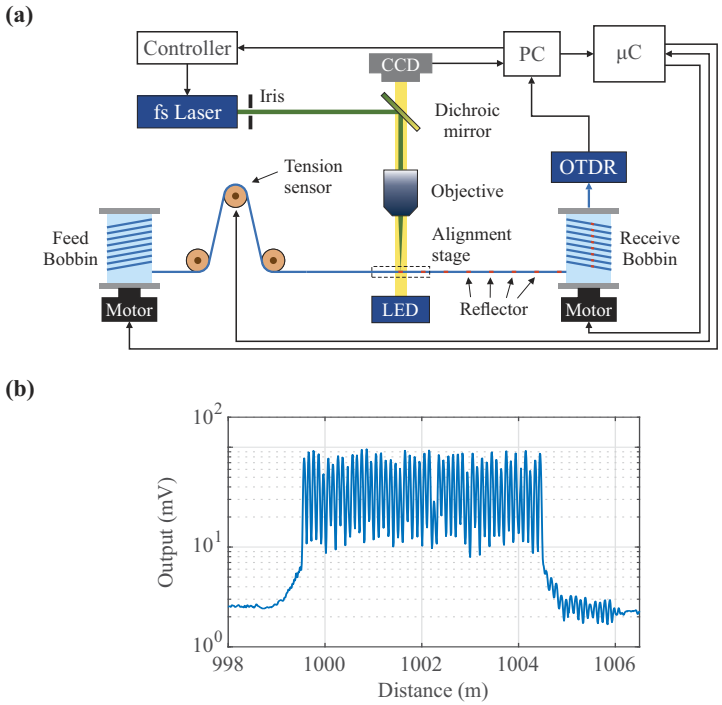


**Fig. 2.** (a) Schematic of the reel-to-reel, automated, fiber inscription set up. (b) The OTDR trace of the ULEB fiber at the far-end of the FUT exhibiting 50 reflectors with an average reflectivity of 14 $dB$ above the intensity of the Rayleigh backscattered light.

OPTICS CONTINUUM

of the objective lens using a multi-axis stage. A pulley arrangement was used to control the fiber tension during the inscription procedure. An *in-situ* OTDR system was used to allow measuring the optical signal during inscription. This allowed to control the reflectivity level at each reflector and achieve a consistency of $\pm 2\,dB$.

The inscription setup was used to write 50 point reflectors with an average reflectance of $-56\,dB$ and a spatial separation of $10\,cm$ in the core of a SSMF through its polymer coating. With each pair of reflectors constituting a single sensing channel, the ULEB fiber, used in this test, had 49 measurement channels. With an inscription speed of under 2 minutes per reflector which includes fiber alignment, reflector inscription, and rewinding, the number of reflectors used for this study was reduced to 50 to keep the fiber fabrication time under 2 hours.

## 4. Results and discussion

Figure 2(b) shows the OTDR trace of the ULEB fiber at the far-end of the FUT. All 50 reflectors with an average reflectance of $-56\,dB$ can be seen in this diagram. 98% of the reflectors exhibited a relatively uniform reflectivity with less than $3\,dB$ variation. Only one reflector had lower than expected reflectance ($28^{\text{th}}$ reflector with $-60\,dB$ reflectance). The oscillation in the OTDR trace that occurs after the reflectors over the spatial interval of $1005\,m - 1006\,m$ can be linked to the pedestal of the probe pulse. Since electrical pulses applied to the SOA for pulse picking were $10\,ns$ long, limited by the speed of the pulse generator, the optical pulses used for interrogating the FUT had $9.5\,ns$ pedestal. Despite $25\,dB$ extinction ratio between the main optical pulse and its pedestal, the interaction between $95\,cm$ pedestal and 9 reflectors give rise to the oscillatory pattern on the OTDR trace.

Figure 3(a) shows the waterfall diagram of the sensing system at the far-end of the sensing fiber. The location and profile of a $30\,Hz$ vibration, which was used as the test signal, can be clearly identified at $L = 1004\,m$ on the diagram. The color bar on the diagram indicates the strain level imposed on the fiber in $\mu\varepsilon$. The fast Fourier transform (FFT) of the strain level along the FUT is shown in the spectrogram of Fig. 3(b). The $30\,Hz$ modulation at $1004.9\,m$ with peak strain level of $29.3\,\mu\varepsilon$ can be identified on this diagram.

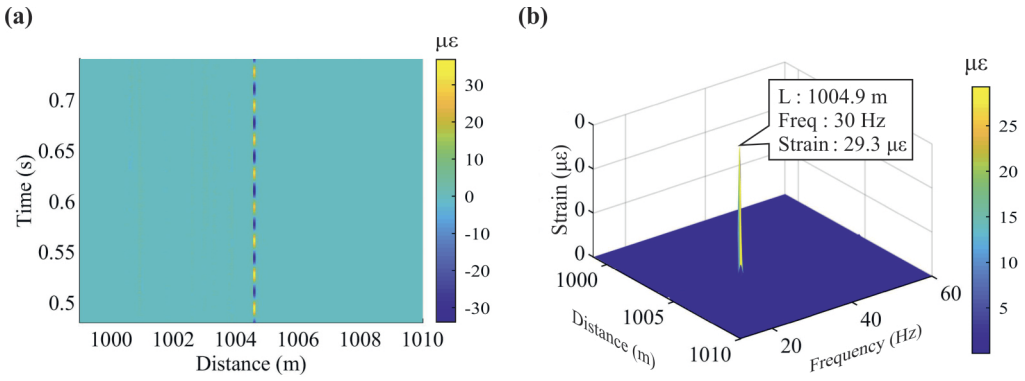


**Fig. 3.** a) Waterfall plot of the sensing system at the far end of the sensing fiber. The horizontal axis represents the distance along the sensing fiber while the vertical axis represents the elapsed time. b) Spectrogram of the system output mapping strain level at the last $25\,m$ of the FUT as a function of frequency. c) 2D cross-section of the waterfall plot showing the strain variation at the the $48^{\text{th}}$ channel of the ULEB fiber as a function of time. d) 2D cross-section of the spectrogram plot, taken perpendicular to the frequency axis at $f = 30\,Hz$, demonstrating the spatial resolution of the system.

OPTICS CONTINUUM

Figure 4(a) shows a 2D cross-section of the waterfall diagram at a fixed location on the FUT, corresponding to the 48$^{th}$ channel of the ULEB fiber, as a function of time. In order to quantify the spatial resolution of the sensor, a 2D cross-section of the spectrogram at $f = 30\,Hz$, is shown in Fig. 4(b). The rising edge of the strain profile, shown in this plot, is 8 $cm$ which is less than the 10 $cm$ spatial resolution of the system dictated by the spacing between the reflectors. This discrepancy is due to the mismatch between the sampling rate of the digitizer that is used to capture the backscattered light and the spacing between the reflectors along the ULEB fiber. With 1.25 $GS/s$ sampling rate, the digitizer acquire one sample every 8 $cm$. Hence, the rise time of the signal appears to be less than the 10 $cm$ spacing between the reflectors.

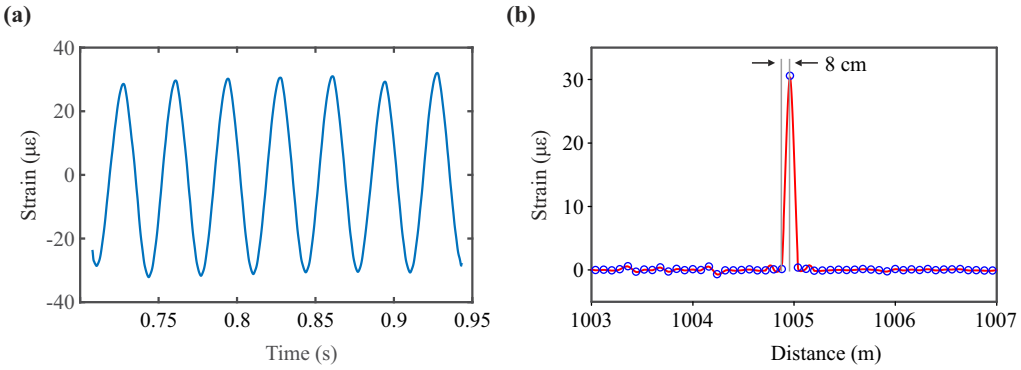


**Fig. 4.** a) 2D cross-section of the waterfall plot showing the strain variation at the the 48$^{th}$ channel of the ULEB fiber as a function of time. b) 2D cross-section of the spectrogram plot, taken perpendicular to the frequency axis at $f = 30\,Hz$, demonstrating the spatial resolution of the system.

In order to assess the noise floor and cross-talk of the sensing arrangement, amplitude spectral densities (ASDs) of the strain levels at the last three channels of the ULEB fiber are shown in Fig. 5(a). The ASD of the strain level at the 48$^{th}$ channel of the ULEB fiber, the channel which is stimulated by the PZT actuator, is represented by the blue trace. The peak at 30 $Hz$ shows the frequency and amplitude of the test signal. The yellow trace shows the ASD of the strain at the 47$^{th}$ channel of the ULEB fiber, a sensing channel before the PZT that has not been disturbed. The noise floor of the system, calculated by averaging the noise from 10 $Hz$ to 1 $kHz$, shows a phase noise of $-29.23$ (re rad/$\sqrt{Hz}$) which corresponds to a strain noise of 1.9 $n\varepsilon/\sqrt{Hz}$. The noise floor is identified by the dashed line on the figure. To assess the cross-talk between the adjacent sensing channels, the ASD of the 48$^{th}$ channel (the channel attached to the PZT) is compared with that of the 49$^{th}$ channel which is represented by the red trace on the plot. The analysis of the frequency peaks on the two traces shows a cross-talk of less than 21 $dB$. With an excess loss of 0.01 $dB$ per 100 reflectors, our analysis shows that replacing the SSMF at the front-end of the FUT with ULEB fiber with 10 $cm$ spacing will not have any notable impact on the noise and cross-talk levels of the sensing system. With previous studies showing the capability of DAS system in measuring 33 $n\varepsilon/\sqrt{Hz}$ vibration along a ULEB fiber at the far-end of 152 $km$ SSMF with total round-trip loss of 60 $dB$ [37], 1 $dB$ excess loss from 1 $km$ long ULEB fiber with 10 $cm$ spacing will have no substantial effect on the sensitivity of the system.

The intra-channel noise and inter-channel cross-talk, observed in the result, can be associated with the pedestal of the probe pulse as discussed earlier. The interaction of the pedestal with other reflectors along the ULEB fiber causes additional light reflection which gets added to the reflected light from the main pulse and causes distortion. Hence, by reducing the duration of pulse picking signal to better match the width of the probe pulse, it is possible to significantly reduce both the noise floor of the system and the cross-talk between different channels. Additionally, the

OPTICS CONTINUUM

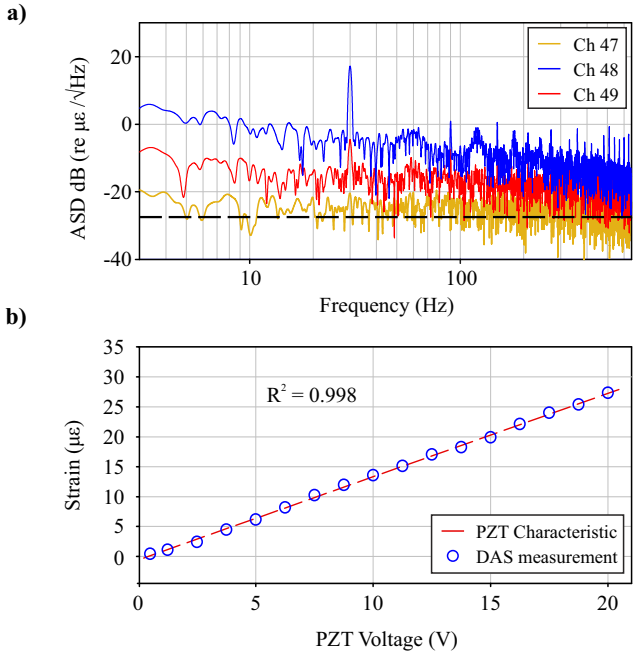


**Fig. 5.** a) Amplitude spectral density (ASD) of the strain levels at the last three channels of the ULEB fiber. The blue trace represents the ASD of the strain level at the 48$^{th}$ sensing channel where the PZT actuator is located. The yellow and red traces represent the ASD of the strain level at 47$^{th}$ and 49$^{th}$ channels of the ULEB fiber, respectively, i.e. the sensing channels just before and just after the PZT. The dashed line at the bottom of the plot represents the noise floor of the sensor. b) The peak strain level measured by the DAS system (blue circles) for 30 $Hz$ sinusoidal test signals at various amplitudes from 0.5 $V$ to 20 $V$. The red dashed line represents the response of the PZT transducer, characterised separately with a Michelson interferometer.

mismatch between the sampling rate of the digitizer and the spatial resolution of the sensing fiber may contribute to the overall noise floor of each sensing channel.

In order to assess the linearity of the system, the sensing setup was used to measure the strain level at channel 48 of the ULEB fiber while increasing the drive voltage applied to the PZT from 0.5 $V$ to 20 $V$. The measurements, represented by blue circles in Fig. 5(b), exhibited a high correlation ($R^2$ = 0.998) with the response of the PZT transducer which was characterized separately using a Michelson interferometer (dashed red line). In addition, the response of the system to vibrations across a wide frequency range from 0.1 $Hz$ to 5 $kHz$ was assessed confirming the linear response of the sensing arrangement.

## 5. Conclusion

In summary, a high resolution DAS system based on ULEB fiber is demonstrated. It is shown that, unlike conventional sensing systems that are based on SSMF or CGEB fibers, the DAS systems that use ULEB fiber as a sensing medium do not experience the trade-off between the spatial resolution and SNR. A ULEB fiber with 50 reflectors and an average reflectance of $-56$ $dB$ is used to demonstrate a DAS with 10 $cm$ spatial resolution at the far-end of 1 $km$ sensing fiber. To fabricate a ULEB fiber with consistent reflectivity, an automated reel-to-reel fiber inscription setup with an *in-situ* OTDR feedback system is developed. A simple sensing arrangement based on a digitizer with 600 $MHz$ bandwidth and an imbalanced MZI is used to achieve this resolution.

OPTICS CONTINUUM

The sensor exhibited a high degree of linearity, a $1.9\,n\varepsilon/\sqrt{Hz}$ ASD noise floor, and a maximum channel cross-talk of less than 21 $dB$. The spatial resolution of the measurement, achieved in this work, was limited by the sampling rate and bandwidth of the digitizer. Using a digitizer with 3 $GHz$ bandwidth and 100 $ps$ probe pulse with sech-squared profile, it is possible to push the spatial resolution of ULEB-based DAS to as low as 1 $cm$.

**Funding.** Royal Academy of Engineering (PoC1920/21, RF1415/14/6); Royal Society (CHL/R1/180350); Natural Environment Research Council (NE/S012877/1, NE/T005890/1).

**Disclosures.** The authors declare no conflicts of interest.

**Data availability.** Data underlying the results presented in this paper are available in Ref. [39].

## References

1. D. Molteni, M. J. Williams, and C. Wilson, "Detecting microseismicity using distributed vibration," First Break. **35**(4), 1 (2017).
2. P. Jousset, T. Reinsch, T. Ryberg, H. Blanck, A. Clarke, R. Aghayev, G. P. Hersir, J. Henninges, M. Weber, and C. M. Krawczyk, "Dynamic strain determination using fiber-optic cables allows imaging of seismological and structural features," Nat. Commun. **9**(1), 2509 (2018).
3. N. J. Lindsey and E. R. Martin, "Fiber-optic seismology," Annu. Rev. Earth Planet. Sci. **49**(1), 309–336 (2021).
4. D. Milne, A. Masoudi, E. Ferro, G. Watson, and L. Le Pen, "An analysis of railway track behaviour based on distributed optical fiber acoustic sensing," Mech. Syst. Signal Process. **142**, 106769 (2020).
5. A. Mateeva, J. Lopez, H. Potters, J. Mestayer, B. Cox, D. Kiyashchenko, P. Wills, S. Grandi, K. Hornman, B. Kuvshinov, W. Berlang, Z. Yang, and R. Detomo, "Distributed acoustic sensing for reservoir monitoring with vertical seismic profiling," Geophys. Prospect. **62**(4), 679–692 (2014).
6. A. Lellouch and B. L. Biondi, "Seismic applications of downhole DAS," Sensors **21**(9), 2897 (2021).
7. A. Masoudi, J. A. Pilgrim, T. P. Newson, and G. Brambilla, "Subsea cable condition monitoring with distributed optical fiber vibration sensor," J. Lightwave Technol. **37**(4), 1352–1358 (2019).
8. Z. W. Ding, X. P. Zhang, N. M. Zou, F. Xiong, J. Y. Song, X. Fang, F. Wang, and Y. X. Zhang, "Phi-OTDR based on-line monitoring of overhead power transmission line," J. Lightwave Technol. **39**(15), 5163–5169 (2021).
9. L. D. Van Putten, A. Masoudi, and G. Brambilla, "100-km-sensing-range single-ended distributed vibration sensor based on remotely pumped erbium-doped fiber amplifier," Opt. Lett. **44**(24), 5925–5928 (2019).
10. S. Liehr, C. Borchardt, and S. Münzenberger, "Long-distance fiber optic vibration sensing using convolutional neural networks as real-time denoisers," Opt. Express **28**(26), 39311–39325 (2020).
11. O. H. Waagaard, E. Rønnekleiv, A. Haukanes, F. Stabo-Eeg, D. Thingbø, S. Forbord, S. E. Aasen, and J. K. Brenne, "Real-time low noise distributed acoustic sensing in 171 km low loss fiber," OSA Continuum **4**(2), 688–701 (2021).
12. A. Hartog, L. Liokumovich, N. Ushakov, O. Kotov, T. Dean, T. Cuny, A. Constantinou, and F. Englich, "The use of multi-frequency acquisition to significantly improve the quality of fiber-optic-distributed vibration sensing," Geophys. Prospect. **66**(S1), 192–202 (2018).
13. Z. Ju, Z. Yu, Q. Hou, K. Lou, M. Chen, Y. Lu, and Z. Meng, "Low-noise and high-sensitivity $\phi$-OTDR based on an optimized dual-pulse heterodyne detection scheme," Appl. Opt. **59**(7), 1864–1870 (2020).
14. Y. Wakisaka, D. Iida, H. Oshida, and N. Honda, "Fading suppression of $\phi$-OTDR with the new signal processing methodology of complex vectors across time and frequency domains," J. Lightwave Technol. **39**(13), 4279–4293 (2021).
15. H. M. Ogden, M. J. Murray, J. B. Murray, C. Kirkendall, and B. Redding, "Frequency multiplexed coherent φ-OTDR," Sci. Rep. **11**(1), 17921 (2021).
16. P. Shrestha, J. H. Kim, Y. Park, and C. G. Kim, "Impact localization on composite wing using 1D array FBG sensor and rms/correlation based reference database algorithm," Compos. Struct. **125**, 159–169 (2015).
17. H. Alexakis, F. D. H. Lau, and M. J. DeJong, "Fiber optic sensing of ageing railway infrastructure enhanced with statistical shape analysis," J. Civ. Struct. Heal. Monit. **11**(1), 49–67 (2021).
18. F. Zhu, Y. Zhang, L. Xia, X. Wu, and X. Zhang, "Improved $\phi$-OTDR sensing system for high-precision dynamic strain measurement based on ultra-weak fiber Bragg grating array," J. Lightwave Technol. **33**(23), 4775–4780 (2015).
19. Y. Wang, P. Lu, S. Mihailov, L. Chen, and X. Bao, "Strain measurement range enhanced chirped pulse φ-OTDR for distributed static and dynamic strain measurement based on random fiber grating array," Opt. Lett. **45**(21), 6110–6113 (2020).
20. C. Li, J. Tang, Y. Jiang, C. Cheng, L. Cai, and M. Yang, "An enhanced distributed acoustic sensor with large temperature tolerance based on ultra-weak fiber Bragg grating array," IEEE Photonics J. **12**(6), 1–8 (2020).
21. C. Li, J. Tang, C. Cheng, L. Cai, and M. Yang, "FBG arrays for quasi-distributed sensing: A review," Photonic Sens. **11**(1), 91–108 (2021).
22. Z. Li, Y. Tong, X. Fu, J. Wang, Q. Guo, H. Yu, and X. Bao, "Simultaneous distributed static and dynamic sensing based on ultra-short fiber Bragg gratings," Opt. Express **26**(13), 17437–17446 (2018).
23. A. Masoudi and T. P. Newson, "High spatial resolution distributed optical fiber dynamic strain sensor with enhanced frequency and strain resolution," Opt. Lett. **42**(2), 290–293 (2017).

OPTICS CONTINUUM


24. S. Feng, T. Xu, J. Huang, Y. Yang, L. Ma, and F. Li, "Sub-meter spatial resolution phase-sensitive optical time-domain reflectometry system using double interferometers," Appl. Sci. **8**(10), 1899 (2018).
25. D. Chen, Q. Liu, and Z. He, "High-fidelity distributed fiber-optic acoustic sensor with fading noise suppressed and sub-meter spatial resolution," Opt. Express **26**(13), 16138–16146 (2018).
26. H. Martins, K. Shi, B. Thomsen, S. Martin Lopez, M. Gonzalez Herraez, and S. Savory, "Real time dynamic strain monitoring of optical links using the backreflection of live PSK data," Opt. Express **24**(19), 22303–22318 (2016).
27. D. Arbel and A. Eyal, "Dynamic optical frequency domain reflectometry," Opt. Express **22**(8), 8823–8830 (2014).
28. J. Li, J. Gan, Z. Zhang, X. Heng, C. Yang, Q. Qian, S. Xu, and Z. Yang, "High spatial resolution distributed fiber strain sensor based on phase-OFDR," Opt. Express **25**(22), 27913–27922 (2017).
29. L. Marcon, A. Galtarossa, and L. Palmieri, "High-frequency high-resolution distributed acoustic sensing by optical frequency domain reflectometry," Opt. Express **27**(10), 13923–13933 (2019).
30. H. Li, Q. Liu, D. Chen, Y. Deng, and Z. He, "High-spatial-resolution fiber-optic distributed acoustic sensor based on $\phi$-OFDR with enhanced crosstalk suppression," Opt. Lett. **45**(2), 563–566 (2020).
31. C. Liang, Q. Bai, M. Yan, Y. Wang, H. Zhang, and B. Jin, "A comprehensive study of optical frequency domain reflectometry," IEEE Access **9**, 41647–41668 (2021).
32. P. S. Westbrook, K. S. Feder, T. Kremp, E. M. Monberg, H. Wu, B. Zhu, L. Huang, D. A. Simoff, S. Shenk, V. A. Handerek, M. Karimi, A. Nkansha, and A. Yau, "Enhanced optical fiber for distributed acoustic sensing beyond the limits of Rayleigh backscattering," iScience **23**(6), 101137 (2020).
33. A. Donko, R. Sandoghchi, A. Masoudi, M. Beresna, and G. Brambilla, "Surpassing the detection limits of current distributed acoustic sensing systems," in *26th International Conference on Optical Fiber Sensor*, (OSA, 2018). Paper WF75.
34. L. Zhang, Z. Yang, N. Gorbatov, R. Davidi, M. Galal, L. Thévenaz, and M. Tur, "Distributed and dynamic strain sensing with high spatial resolution and large measurable strain range," Opt. Lett. **45**(18), 5020–5023 (2020).
35. J. Xiong, Z. Wang, J. Jiang, B. Han, and Y. Rao, "High sensitivity and large measurable range distributed acoustic sensing with Rayleigh-enhanced fiber," Opt. Lett. **46**(11), 2569–2572 (2021).
36. B. Redding, M. J. Murray, A. Donko, M. Beresna, A. Masoudi, and G. Brambilla, "Low-noise distributed acoustic sensing using enhanced backscattering fiber with ultra-low-loss point reflectors," Opt. Express **28**(10), 14638–14647 (2020).
37. A. Masoudi, M. Beresna, and G. Brambilla, "152 km-range single-ended distributed acoustic sensor based on inline optical amplification and a micromachined enhanced-backscattering fiber," Opt. Lett. **46**(3), 552–555 (2021).
38. L. D. van Putten, A. Masoudi, J. Snook, and G. Brambilla, "Numerical modelling of a distributed acoustic sensor based on ultra-low loss-enhanced backscattering fibers," Sensors **21**(20), 6869 (2021).
39. A. Masoudi, "Data set for '10 cm special resolution distributed acoustic sensor based on ultra low-loss enhanced back-scattering fiber'," University of Southampton Institutional Repository 2022, https://doi.org/10.5258/SOTON/D2116.